Postretinal Structure and Function in Severe Congenital Photoreceptor Blindness Caused by Mutations in the *GUCY2D* Gene

Geoffrey K. Aguirre,[1] Omar H. Butt,[1] Ritobrato Datta,[1] Alejandro J. Roman,[2] Alexander Sumaroka,[2] Sharon B. Schwartz,[2] Artur V. Cideciyan,[2] and Samuel G. Jacobson[2]

[1]Department of Neurology, Perelman School of Medicine, University of Pennsylvania, Philadelphia, Pennsylvania, United States
[2]Department of Ophthalmology, Perelman School of Medicine, University of Pennsylvania, Philadelphia, Pennsylvania, United States

Correspondence: Geoffrey K. Aguirre, Department of Neurology, Perelman School of Medicine, University of Pennsylvania, Philadelphia, PA 19104, USA; aguirreg@mail.med.upenn.edu.

Submitted: July 28, 2016
Accepted: December 27, 2016

Citation: Aguirre GK, Butt OH, Datta R, et al. Postretinal structure and function in severe congenital photoreceptor blindness caused by mutations in the *GUCY2D* gene. *Invest Ophthalmol Vis Sci*. 2017;58:959–973. DOI:10.1167/iovs.16-20413

Purpose. To examine how severe congenital blindness resulting from mutations of the *GUCY2D* gene alters brain structure and function, and to relate these findings to the notable preservation of retinal architecture in this form of Leber congenital amaurosis (LCA).

Methods. Six *GUCY2D*-LCA patients (ages 20–46) were studied with optical coherence tomography of the retina and multimodal magnetic resonance imaging (MRI) of the brain. Measurements from this group were compared to those obtained from populations of normally sighted controls and people with congenital blindness of a variety of causes.

Results. Patients with *GUCY2D*-LCA had preservation of the photoreceptors, ganglion cells, and nerve fiber layer. Despite this, visual function in these patients ranged from 20/160 acuity to no light perception, and functional MRI responses to light stimulation were attenuated and restricted. This severe visual impairment was reflected in substantial thickening of the gray matter layer of area V1, accompanied by an alteration of resting-state correlations within the occipital lobe, similar to a comparison group of congenitally blind people with structural damage to the retina. In contrast to the comparison blind population, however, the *GUCY2D*-LCA group had preservation of the size of the optic chiasm, and the fractional anisotropy of the optic radiations as measured with diffusion tensor imaging was also normal.

Conclusions. These results identify dissociable effects of blindness upon the visual pathway. Further, the relatively intact postgeniculate white matter pathway in *GUCY2D*-LCA is encouraging for the prospect of recovery of visual function with gene augmentation therapy.

Keywords: visual cortex, functional imaging, retinal degeneration

Congenital blindness from eye disease produces a well-documented set of structural and functional changes to the human brain. At a macroscopic level, the postretinal pathway from the optic chiasm to the pericalcarine white matter is reduced in size.[1–3] This reduction in size is accompanied by a change in the organization of postgeniculate white matter as measured by diffusion tensor imaging.[4,5] Blindness also produces a thickening of the gray matter layer of visual cortex,[4,6,7] perhaps reflecting altered synaptic pruning during cortical maturation.[8,9] This thickening is related to functional alterations of the occipital cortex in blindness, most notably the development of "cross-modal" responses in which occipital areas respond to nonvisual stimulation.[10–12]

These effects upon the brain could result from one or more properties of blindness. While the rudimentary organization of the visual pathway is established prenatally,[13] congenital blindness removes the formed visual input that is used to refine the system.[14] Ophthalmologic disease that disrupts the retina also deprives the visual system of intrinsic signals from the retinal ganglion cells (RGCs), including spontaneous retinal activity[15] and neurotrophic effects.[16] Consistent with this dual mechanism model, animal studies of visual deprivation find that the loss of formed visual input alters the brain in ways that are different from the loss of RGCs from enucleation.[17,18] There have been limited efforts to separate these influences in humans.[19] A key challenge is the rarity of patients with severe congenital vision loss who nonetheless have a structurally normal retina. Patients with isolated anterior segment disease (e.g., cataracts) are generally treated in infancy (although see Ref. 20). Consequently, most adults with congenital blindness have experienced a loss of both formed visual input and intrinsic RGC function.

This dissociation of retinal structure and visual function in adulthood is found in people with certain forms of Leber congenital amaurosis (LCA), a congenital retinal blindness that has become a target of gene augmentation therapy.[21,22] In particular, mutations in the *GUCY2D* gene interrupt the phototransduction pathway in retinal photoreceptors, causing severe vision loss.[23–25] Visual acuity in *GUCY2D*-LCA is generally 20/200 or worse,[25] and retinal electrophysiology (by electroretinogram) indicates profound photoreceptor dysfunction.[24] Despite this severe impairment in visual function, *GUCY2D*-LCA is remarkable for the relatively preserved structure of the retina. When viewed with the cross-sectional retinal imaging modality optical coherence tomography (OCT), there is generally normal photoreceptor laminar architecture.[24,26]

Here, we tested if the striking dissociation of retinal structure and function in *GUCY2D*-LCA also produces a dissociation in the postretinal brain alterations that accompany blindness. We obtained multimodal, magnetic resonance imaging (MRI) of the brain for a group of six LCA patients with *GUCY2D* mutations and severe, congenital vision loss; a substantial population to be studied with this rare clinical entity. Measurements from this group were compared to measurements previously made in sighted subjects, and in people with congenital blindness from causes that have disrupted retinal structure.[27–32] We first confirmed with OCT that *GUCY2D*-LCA has preserved retinal structure, and with visual testing and functional MRI that a severe visual impairment is present. We then examined the macroscopic structure of the postretinal visual system, the microscopic coherence of the postgeniculate white matter pathway, and the functional properties of visual cortex in response to auditory stimulation and in the organization of spontaneous neural activity.

Table. *GUCY2D*-LCA Patients

Patient/ Sex	Age at Visit, y	Allele 1	Allele 2	Eye	Visual Acuity*
P1†/F	20	IVS18+1 G>C	Ser248Trp	RE	20/400
				LE	20/500
P2†/M	23	Arg768Trp	Arg768Trp	RE	HM
				LE	CF
P3†/F	24	Arg768Trp	Arg1091X	RE	20/160
				LE	20/250
P4†/F	37	Leu865 del1bp	Met476 ins10bp	RE	NLP
				LE	BLP
P5/F	44	Ser448X	Ser448X	RE	HM
				LE	LP
P6/F	46	Ser448X	Ser448X	RE	20/320
				LE	20/250

HM, hand motion; CF, count fingers; NLP, no light perception; BLP, bare light perception; LP, light perception.

* Best-corrected visual acuity.

† Previously reported.[24]

Methods

Subjects

Six *GUCY2D*-LCA patients were studied (Table; five females, one male, ages 20–46). All subjects were studied at the University of Pennsylvania. Informed consent was obtained; procedures followed the Declaration of Helsinki and had institutional review board approval. Magnetic resonance imaging and anatomic and functional data from these six subjects were compared to the same measures from a set of 59 normally sighted controls (24 men, 35 women, mean age 39 ± 14 SD) and a comparison population of 40 people with congenital blindness (17 men, 23 women, mean age 40 ± 18 SD). The sighted and comparison blind populations have been the subject of prior reports.[27–32] The comparison blind population was composed of people with congenital blindness from causes that disrupted retinal structure, including anophthalmia, microophthalmia, retinopathy of prematurity, congenital optic atrophy, congenital glaucoma, and forms of LCA known to disrupt the neural retina.[28] Seven of the subjects in the blind population had some residual light perception; the remaining 33 had no light perception.

Retinal Imaging

Spectral-domain OCT (SD-OCT) was performed (RTVue-100; Optovue, Inc., Fremont, CA, USA). Optical coherence tomography scans were formed by laterally sampling longitudinal reflectivity profiles (LRPs) in predefined patterns forming lines, rasters, or circles. The horizontal meridian through the fovea was studied with overlapping line scans (4.5 or 9 mm long, 4091 LRPs each). Circular scans of 3.4-mm diameter centered on the optic nerve head were used to quantify the peripapillary retinal nerve fiber layer (NFL).[33,34]

The OCTs were analyzed with custom programs (MatLab 7.5; MathWorks, Natick, MA, USA) after the LRPs were aligned by straightening the major RPE reflection.[35] The thickness of the following retinal sublaminae (from vitreous to choroid) was quantified in patients and normal subjects: hyperreflective NFL; hyporeflective ganglion cell layer (GCL); and hyporeflective outer nuclear layer (ONL). Signal peak assignments were based on previous publications[36–39]; the OCT sublamina have been shown to correspond to histologically defined layers.[20,40,41] Of note, our ONL was defined between the boundary immediately vitread to the outer limiting membrane scattering peak where the maximum of the local slope is reached and the boundary immediately sclerad to the outer plexiform layer peak that is closest to the hyposcattering inner nuclear layer. This definition of ONL includes the anatomic layers of photoreceptor cell nuclei as well as the Henle fibers[42]; in the remainder of the text we therefore refer to this as the ONL+ layer. Use of directional OCT to differentiate between the two sublayers[43,44] was not possible in these *GUCY2D*-LCA patients with unstable fixation.

Structural MRI Acquisition and Analysis

A T1-weighted, three-dimensional magnetization-prepared rapid gradient-echo (MPRAGE) image was acquired for each subject using a 3-Tesla Siemens Trio with an 8-channel Siemens head coil (Berlin, Germany): 160 slices, 1 × 1 × 1 mm, repetition time (TR) = 1.62 s, echo time (TE) = 3.87 ms, inversion time (TI) = 950 ms, field of view (FoV) = 250 mm, flip angle = 15°.

The FreeSurfer (v5.1) toolkit (http://surfer.nmr.mgh.harvard.edu/; in the public domain)[45–48] was used to process anatomic MPRAGE images and construct white matter, pial, inflated, and spherical brain surfaces. Briefly, this processing includes spatial inhomogeneity correction, nonlinear noise reduction, skull stripping,[49] subcortical segmentation,[50,51] intensity normalization,[52] surface generation,[45,46,53] topology correction,[54,55] surface inflation,[46] registration to a spherical atlas,[47] and thickness calculation.[48] This approach matches morphologically homologous cortical areas based on the cortical folding patterns with minimal metric distortion[47] and allows sampling at subvoxel resolution and detection of cortical thickness differences at the submillimeter level.[48] Cortical thickness was estimated at each point across the cortical mantle by calculating the distance between the gray–white matter boundary and the cortical surface.

As described previously,[28] multiple regions of interest (ROIs) were defined along the visual pathway using automated methods and were subjected to visual inspection and manual correction of any errors in segmentation. Regions included the optic chiasm (identified through automated subcortical segmentation using FreeSurfer),[51] lateral geniculate nucleus (defined within Montreal Neurologic Institute [MNI] space using the Jülich atlas),[56–58] pericalcarine white matter (demarcated using the using the Destrieux 2009 atlas segmenta-

Investigative Ophthalmology & Visual Science

tions),[59] and primary visual cortex (demarcated with reference to cortical surface topology).[60–62]

From these ROIs, a total of eight anatomic measures (left and right V1 cortical thickness, left and right V1 surface area, left and right pericalcarine volume, optic chiasm volume, and lateral geniculate nucleus [LGN] volume) were extracted from the MPRAGE image for each subject. V1 cortical thickness was estimated at each point across the cortical mantle by calculating the distance between the gray–white matter boundary and the cortical surface using FreeSurfer. These measures were then averaged across the entire surface of V1. V1 surface area was defined as the sum of the area (mm^2) enclosed by all vertices comprising the striate (V1) cortex at the gray–white matter boundary. Pericalcarine white matter, optic chiasm, and splenium volumes were also estimated using FreeSurfer. Volume of the LGN was estimated using tensor-based morphometry (TBM). Tensor-based morphometry calculates the Jacobian determinant for each voxel of the deformation field that relates an individual brain to the common template brain in MNI space, thus providing a measure of tissue growth or shrinkage for each voxel of the brain.[63,64] The mean Jacobian determinant of the deformation field was extracted for the LGN ROI. This indirect index (as opposed to direct volumetric measurement) was used as there are no clear anatomic boundaries that define the LGN within a T1 image.

Following a previously described procedure,[28] each measurement was then adjusted to account for individual differences in age, sex, and overall brain size (whole-brain cortical thickness, surface area, supratentorial volume, and intracranial volume). A prior analysis[28] of 112 blind and sighted people yielded parameter estimates of the relationship between each local measurement in the visual pathway and the categorical effect of sex, the linear and higher-order polynomial (quadratic and cubic) effect of age, and the linear and higher-order polynomial effect of the whole-brain measures. This prior analysis found that vision status (blind or sighted) did not interact with these effects. The set of anatomic measurements obtained from each *GUCY2D*-LCA subject were adjusted to remove the influence of individual differences in age, sex, and whole-brain size using these previously obtained parameter estimates.

Separate measurements from the left and right hemisphere for cortical thickness, V1 surface area, and pericalcarine volume were averaged, given prior findings that measurements in the two hemispheres are highly correlated in both blind and sighted people.[28]

Diffusion Tensor Imaging Acquisition and Analysis

Diffusion tensor imaging (DTI) data were collected as a single $b = 0$ volume followed by 30 ($b = 1000$ s/mm^2) volumes with different gradient directions: FoV = 220 mm, matrix = 128 × 128 (1.72 × 1.72-mm voxel resolution in plane), TR = 6300 ms, TE = 85 ms, 53 slices with thickness 2.1 mm, interleaved. Diffusion tensor imaging data from some subjects in the sighted and comparison blind populations were obtained using a slightly different set of parameters. These details, and tests demonstrating that the variation in scanning protocol does not impact measurement of fractional anisotropy from the visual pathway, have been provided previously.[28]

Each diffusion-weighted volume was skull stripped and coregistered to the first $b = 0$ volume using a rigid affine transformation to correct for distortion caused by eddy-current effects and simple head motion using FMRIB's software library and diffusion toolbox v2.0 (FSL, http://www.fmrib.ox.ac.uk/fsl/; in the public domain). The diffusion tensor of each voxel was calculated by a linear least-squares fitting algorithm.[65] After rendering the diffusion tensor along the diagonal, the three diffusion tensor eigenvalues were obtained (mean diffusivity, axial diffusivity, and radial diffusivity). Fractional anisotropy (FA) of each voxel was derived based on the three eigenvalues. The FA was used as a measure of the degree of diffusion anisotropy. Fractional anisotropy varies between zero, representing isotropic diffusion, and unity, in the case of the diffusion restricted to a single direction. The individual diffusion-weighted images from each subject were coregistered to subject-specific anatomy in FreeSurfer using FSL-FLIRT with six degrees of freedom under a FreeSurfer wrapper (bbregister). The resulting registration matrices were used to transform the FA maps to FreeSurfer anatomic space and also to transform ROIs estimated in FreeSurfer space to subject-specific diffusion space.

The splenium and forceps of the posterior part of corpus callosum were defined as a conjoint region. The FreeSurfer segmentation routine divides the corpus callosum into five equally spaced ROIs along the anterior–posterior axis; the splenium was defined in each subject as the most posterior ROI. Independently, the splenium of the corpus callosum in MNI space was identified using the Johns Hopkins University DTI-based white matter atlases.[66,67] The splenium in MNI space technically consists of the splenium and forceps. This ROI in MNI space was warped back to individual subject anatomic space in FreeSurfer using diffeomorphic warping in the Advanced Normalization Tools (ANTs) (http://stnava.github.io/ANTs/; in the public domain). All of the voxels from each region were added to a single, unified region. Visual inspection was conducted for each subject to remove any voxels from the segmentation that might overlap with gray matter or the ventricles. The optic radiations were identified in MNI space using the Jülich histologic atlas[56–58] and warped to individual subject space in FreeSurfer using diffeomorphic warping in ANTs. Any non-white matter voxels were removed by visual inspection.

The mean FA value in the splenium and optic radiations was obtained from the combination of these ROIs in each subject. Derivation of the FA value from this combined ROI obviated the need to segment the tracks attributable to the forceps of the splenium and the optic radiations.

BOLD fMRI Acquisition

BOLD functional MRI (fMRI) data were obtained over 44 axial slices with 3-mm isotropic voxels in an interleaved fashion with 64 × 64 in-plane resolution, FoV = 192 mm, TR = 3000 ms, TR = 30 ms, flip angle 90°. Individual scans (described in detail below) were collected during light stimulation, auditory stimulation, and a "rest" condition during which subjects remained in darkness with eyes closed. For all scans, stray light was minimized using opaque shades and covering light sources, and head motion was minimized with foam padding. Continuous pulse oximetry was recorded during the "rest" scanning sessions.

Light Stimulation

Subjects were dark-adapted prior to scanning. During functional scanning, subjects were presented with a white rectangular screen of uniform luminance that flickered at 5 Hz for 30-second periods, alternating with 30-second periods of darkness. The stimulus was presented using a liquid crystal display (LCD) projector equipped with a long-throw lens that was back-projected onto a Mylar screen. The screen subtended 28° × 18° of visual angle, although light reflected within the bore of the scanner made the effective width of the stimulus considerably larger. During the 30-second periods of darkness,

Investigative Ophthalmology & Visual Science

the projector lens was physically covered with opaque material, thereby increasing stimulus contrast. The maximum screen luminance was measured and found to be 3.75 log cd/m^2. Stimulus intensity could be varied by interposing neutral density filters in the light path. The *GUCY2D*-LCA subjects were studied with two scans of 140 TRs each during stimulation with a −1.8 log stimulus and two scans at the maximum stimulus intensity. The data from the *GUCY2D*-LCA subjects were compared with previous measurements made from nine normally sighted subjects (age range, 20–42), each of whom was studied with two scans of −3 log intensity.[32] In the data from this prior report, measurements were also made from some subjects at higher intensity levels, but not all subjects could tolerate the stimulus. Consequently, we present the −3 log unit data that were obtained for every subject.

Auditory Stimulation

Functional MRI data were collected while subjects listened to auditory sentences and performed semantic judgments. These data were collected from only five of the six *GUCY2D*-LCA patients, as one patient (P5) did not speak English. During BOLD fMRI scanning, subjects listened to 30-second blocks of sentences of the form "The [noun] is [adjective]" or "The [noun] is [present participle]" and reported by button press the infrequent occurrence of a sentence with an implausible or unusual relationship between the words (e.g., "the table was grunting"). During other periods, the subject listened to these sentences played in reverse or to white noise. The subject was in darkness during the scan and was asked to keep the eyes closed. These same measurements from 19 sighted and 33 blind subjects have been reported previously.[28] We measured the joint response to forward and reverse sentences as compared to the white noise control, as this contrast was previously found to produce the largest difference in visual cortex response between the blind and sighted.[28]

Resting State

Functional MRI data were collected while subjects rested with eyes closed in the scanner in darkness. No time-varying stimulation was provided during scanning, and stray light sources were minimized in the scanner room by covering instrument panels and blocking the observation windows. The *GUCY2D*-LCA group participated in three 7.5-minute scans. Data from a single 7.5-minute scan from each of 22 sighted and 25 blind subjects have been reported previously.[29,30]

BOLD fMRI Data Analysis

The analysis approach taken for each type of BOLD fMRI measure has been described previously.[27,29,30,32] Briefly, the echoplanar BOLD fMRI data were sinc interpolated in time to correct for slice acquisition sequence, and motion-corrected with a six-parameter, least-squares, rigid body realignment to the first functional image. The echoplanar data in subject space were then coregistered to subject-specific anatomy in FreeSurfer using FSL-FLIRT with six degrees of freedom under a FreeSurfer wrapper (bbregister). This coregistration step allows volumetric data from each subject to be mapped to the left and right hemispheric surfaces for each subject.

For the light and auditory stimulation scans, covariates of interest were modeled as a simple boxcar and convolved with a standard hemodynamic response function.[68] Covariates of no interest included global signal and "spikes." The latter were identified by automated analysis (time points with excursions of greater than 3 SD from the mean) and visual inspection, and then modeled as impulses. The beta effect for each covariate (expressed as percentage signal change) was derived at each voxel. The volumetric beta maps of percentage signal response to light stimulation, and the combined effect of forward and reverse sentences versus white noise, were derived for each subject and then projected to the cortical surface. To allow across-subject aggregation, individual beta maps were resampled to the FreeSurfer template surface pseudo-hemisphere using the FreeSurfer spherical registration system.[47,69]

Following a previously described approach,[32] light stimulation data were analyzed within a cortical surface template for visual areas V1, V2, and V3.[60,61] Cortical maps of BOLD fMRI effect size were registered to a surface atlas that maps each vertex on the cortical surface to its corresponding visual field location. Response maps for V1, V2, and V3 were obtained out to 48° and averaged. Effect size values are given for each visual field point only if there was a $P < 0.05$ (vertex-wise) effect in at least one of the corresponding cortical locations across the three visual areas.

Auditory stimulation data were smoothed on the cortical surface using a 10-mm full width at half-max (FWHM) isotropic Gaussian kernel. The region-of-interest analysis examined the effect of auditory stimulation within area V1.

Rest-state data were analyzed following a previously described approach.[29] Time-series data from the rest scans were projected to the cortical surface and then spatially smoothed using a 2-mm FWHM, isotropic kernel, and band-pass filtered in time to retain frequencies between 0.01 and 0.08 Hz.[70,71] The effect of nuisance covariates (including cardiac and pulmonary cycles) was regressed from the data as previously described.[29] Anatomic ROIs corresponding to the dorsal and ventral halves of V1, V2, and V3 were defined using a cortical surface template of retinotopy.[60,61] All ROIs excluded the border between regions (defined as ±10° polar angle from the vertical or horizontal meridian between visual areas). For each subject, the Pearson's correlation of the mean resting signal (defined as the average signal of all vertices comprising a given region) between each pair of regions was obtained within a given hemisphere. Each pairwise visual quadrant correlation provided one cell of a resulting 6×6 correlation matrix. Similarly, the Pearson's correlation of the mean resting signal between each pair of regions across hemispheres was obtained. Following a Fisher's r-to-z transformation, one ipsilateral correlation matrix (an average of the right and left hemisphere correlation matrices) and one between-hemisphere correlation matrix were generated for each subject. Cells of the correlation matrices that corresponded to pairings of regions with the same quarter-field representation (termed "hierarchical") were averaged and compared to the average of cells that correspond to pairs of regions from the same cortical visual area (e.g., V1 or V2) but that represent different quarter fields (termed "homotopic"). Results from each *GUCY2D*-LCA subject were averaged across the three scans prior to conducting between-group comparisons.

Results

Minimal Alteration of Retinal Microstructure

We first studied the in vivo histology of the retina by OCT in six *GUCY2D*-LCA patients (Table) and compared the results to normal retinal structure (Fig. 1). An OCT cross section from the normal central retina through the fovea has hyporeflective nuclear layers separated by hyperreflective laminae originating

Investigative Ophthalmology & Visual Science

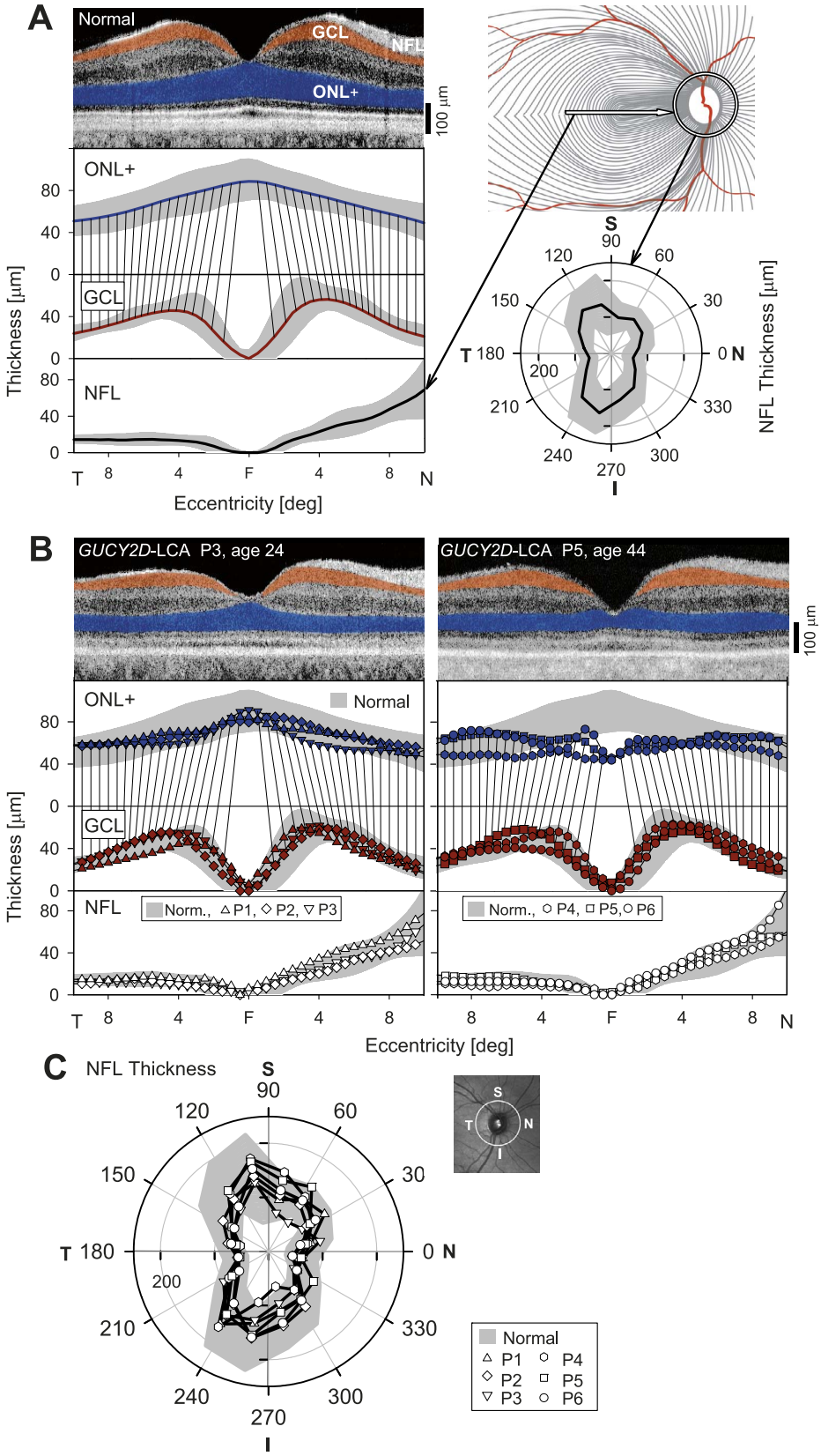

Figure 1. Retinal ganglion cell and nerve fiber layer integrity in *GUCY2D*-LCA. (**A**) *Left*: Cross section by OCT across the horizontal meridian through the fovea; cellular layers (ONL+, *blue*; GCL, *orange*) are highlighted in a normal 28-year-old subject. Thickness of ONL+, GCL, and NFL along the horizontal meridian in normal subjects and the relationship due to foveal anatomy (*shaded areas*, mean ± 2 SD; $n = 12$, ages 8–48). *Right*, *upper*: Schematic of NF distribution in the central retina. *Line* indicates where the horizontal OCT cross section was taken to quantify NFL thickness (*lower left*). The peripapillary region for circular scans and polar plots of NFL thickness is also indicated (normal subjects are *shaded area*, mean ± 2 SD; $n = 15$, ages 8–48). N, nasal; S, superior; T, temporal; I, inferior. (**B**) *Upper*: Cross-sectional OCT scans and highlighted cellular layers in two

Investigative Ophthalmology & Visual Science

representative patients with *GUCY2D*-LCA who participated in the MRI studies. *Lower*: Quantitation of ONL+, GCL, and NFL across the horizontal meridian in six patients with *GUCY2D* mutations. (**C**) Polar plots of NFL thickness in the patients compared to normal limits (*gray shading*). *Inset*: location of the circular peripapillary scan.

from synapses or outer segments (Fig. 1A, upper left). Photoreceptor and ganglion cell (GC) nuclear layers are highlighted (ONL+, blue; GCL, orange), and thickness measurements of the two laminae for a group of normal subjects are shown (Fig. 1A, lower left). There is normally an eccentric displacement of GCs,[72] and this is illustrated by lines connecting corresponding eccentricities on ONL+ and GCL thickness profiles.

The NFL is composed of axons leading from the GCs to the optic nerve head. Quantitation of NFL thickness was performed in two ways, as shown on the schematic of the course of the nerve fibers (Fig. 1A, upper right).[34] First, NFL thickness was measured across the horizontal meridian, and second, as a circular scan around the optic nerve head. Normal statistics and results from the representative subject are shown for the horizontal scan (Fig. 1A, lowest left) and for the circular OCT scan capturing all regions around the optic nerve head on a polar plot (Fig. 1A, lower right).

The ONL+ thicknesses in *GUCY2D*-LCA were significantly different from normal (*t*-test, $P < 0.001$); there were no abnormalities for GCL ($P = 0.07$) or for two measures of NFL ($P = 0.15$ and $P = 0.07$). As the ONL+ differences from normal were small (mean value 63.1 μm in *GUCY2D*-LCA versus 71.5 μm in normal) and the number of patients was limited, we considered variation of results in individual patients. Patient (P) 3 at age 24 represents patients with ONL+, GCL, and NFL layers appearing qualitatively similar to normal across the scanned retinal regions (Fig. 1B, left). Patient 5 at age 44, on the other hand, shows a small reduction of ONL+ thickness in the central few degrees; beyond this central region, the ONL+ appears similar to normal. The GCL and NFL also appear similar to normal across the entire region. Upon quantitative locus-by-locus analyses, three patients (P1, P2, and P3, ages 20–24 years) show ONL+, GCL, and NFL thicknesses that fall within normal limits across the horizontal meridian (Fig. 1B, left). In contrast, the other three patients (P4, P5, and P6, ages 37–46 years) show partial thinning of the ONL+ localized to near the central few degrees. The ONL+ thickness outside the center and GCL and NFL thicknesses throughout the sampled retina are within the normal limits (Fig. 1B, right). Of note, parafoveal GCL thickness that would be expected to contain displaced cells postreceptoral to centrally lost photoreceptors was within normal limits in these patients across all sampled locations. The circular scan measurements of NFL thickness were also within normal limits in all six patients across all sampled locations (Fig. 1C). In summary, *GUCY2D*-LCA patients displayed normal inner retinal and minimally abnormal outer retinal microstructure, especially considering the severe visual dysfunction.

Reduced Cortical Responses to Achromatic Flicker

GUCY2D-LCA patients can have retained rod function, albeit with reduced sensitivity. Cone function tends to be more severely affected.[24] Visual acuity in this group of *GUCY2D*-LCA patients ranges from 20/160 to no light perception (Table).

We expected this impairment in visual function to manifest as diminished visual cortex responses to light stimulation. Following dark adaptation, we obtained a BOLD fMRI measure of neural activity from visual areas V1 to V3 for the *GUCY2D*-LCA patients while they viewed a wide-field, spatially uniform stimulus that was flickering at 5 Hz. The response at two luminance levels was obtained. The BOLD signal during these 30-second periods of stimulation was contrasted with that during 30-second periods of darkness. These responses were compared to previously obtained measurements from normally sighted people, made at a lower luminance level of stimulation for subject comfort.[27]

We investigated how the cortical response to light differed as a function of position in the visual field. Using a cortical template of retinotopic organization,[60] we projected the BOLD fMRI response across cortical areas to a visual field representation (Fig. 2A). The responses from areas V1, V2, and V3 were averaged. Control subjects were studied with stimulation at −3 log units intensity. An essentially uniform BOLD response across the visual field representation is found in control subjects (six of nine subjects shown as examples, including the subject with the largest, C2, and smallest, C3, response). In comparison, there is an attenuation and constriction of response for the *GUCY2D*-LCA population (Fig. 2B), despite their being presented with light levels higher than shown for the controls (−1.8 and 0 log units). There was variability in individual patient responses. For P1, P6, and P3, the patients with better visual acuities (Table), there was a relationship between mapped cortical activity and cone vision by cone-specific perimetry.[24] Patient 3 had the best visual acuity and had measurable, albeit severely reduced, cone vision across the central 40° of visual field. P1 and P6 had more reduced visual acuity, and their cone vision was detectable only in a few central field loci. The remaining three patients had no measurable cone vision but varying degrees of rod-mediated vision.[24]

Alteration of Postchiasmal Anatomy

Blindness is known to produce numerous macroscopic changes to brain anatomy. We examined if changes in brain structure are present in blindness from *GUCY2D*-LCA, and if some aspects of the visual pathway are more altered than others. We obtained five measures (Fig. 3) of postretinal brain anatomy, averaged across the two hemispheres (where applicable). The measurements from the *GUCY2D*-LCA group were compared to previously reported measurements from sighted controls and a group of people with congenital blindness.[28] Unlike *GUCY2D*-LCA, vision loss in the comparison blind group was from one or more processes that disrupt the structure of the retina (e.g., anophthalmia, retinopathy of prematurity, retinitis pigmentosa, congenital glaucoma). The data from each subject were adjusted to account for individual differences in age, sex, and overall variation in brain size and surface area.

We conducted a Kruskall-Wallis test to determine if there was an effect of group on each of the five anatomic measures. For every measure, there was a highly significant overall effect of group (χ^2 [2 df] = 17.4, $P = 0.00016$ for the measure of V1 thickness; all other measures χ^2 [2 df] > 30, $P < 2 \times 10^{-7}$). As has been reported previously,[28] and consistent with multiple prior studies,[1–4,7,73] a significant alteration in brain anatomy is observed for all five measurements in the population of congenitally blind subjects as compared to the sighted ($P = 0.0039$ for V1 thickness; all other *P* values $< 2 \times 10^{-7}$, using the Tukey-Kramer correction for the multiple follow-up comparisons in this and all subsequent tests). Compared to the sighted, the comparison blind population has a smaller optic chiasm,

Investigative Ophthalmology & Visual Science

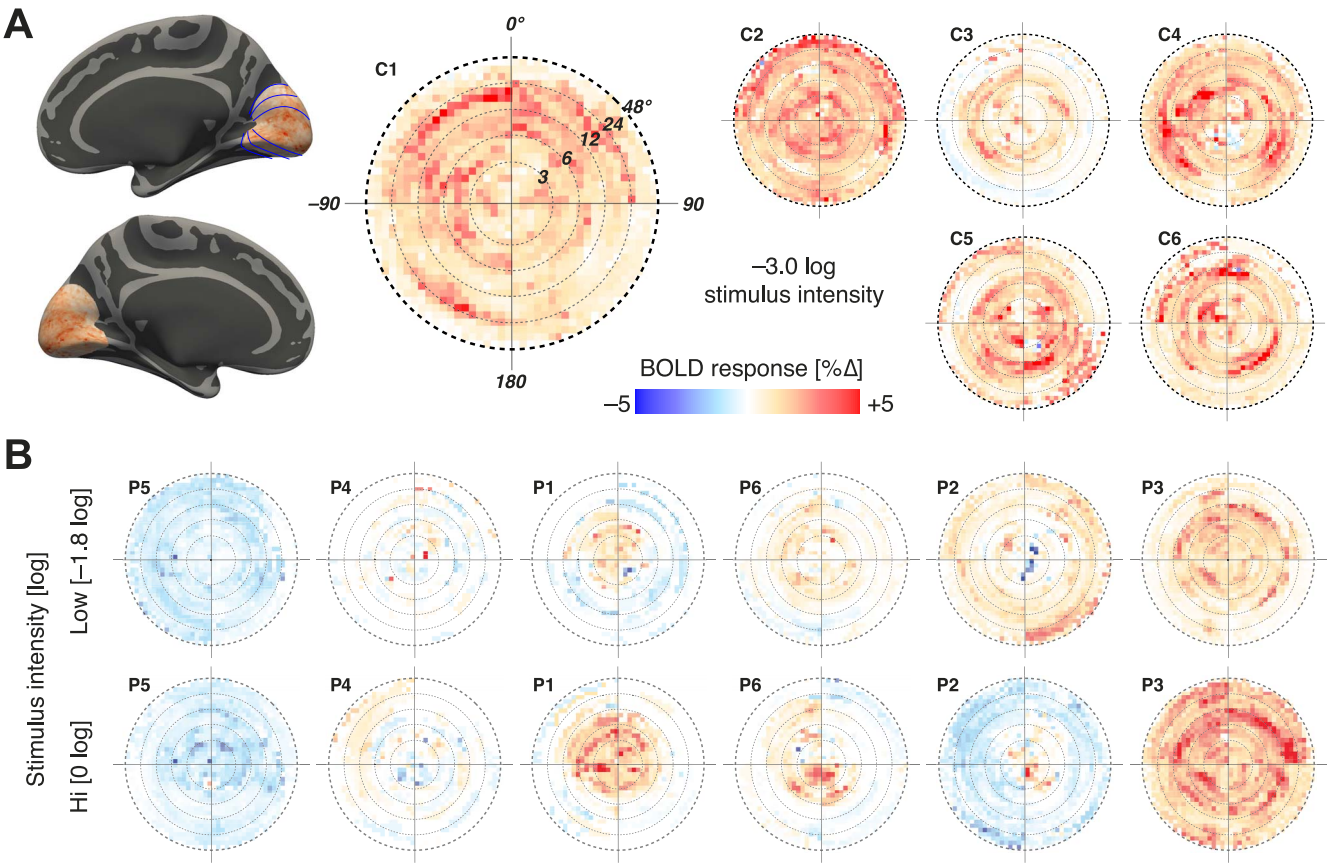

Figure 2. Visual field projections of cortical response. (**A**) *Left*: The cortical response within visual areas V1 to V3 to stimulation at –3.0 log intensity is shown for a control observer (C1). The borders of visual areas are shown with *thin blue lines*. This cortical response (averaged across visual areas) is projected to a visual field representation with logarithmic eccentricity spacing. A roughly uniform, positive response to the stimulus is seen. The same measure for five other control subjects (C2–C6) is shown to the *right*. (**B**) The same visual field projection is shown for the six *GUCY2D*-LCA observers (P1–P6), at two stimulus intensity levels (–1.8 log and 0 log), each of which is higher than used for the controls. Subjects ordered by the relative magnitude of response.

lateral geniculate nucleus, pericalcarine white matter, and surface area of the primary visual cortex (Fig. 3). The gray matter layer of the primary visual cortex is thickened in the blind as compared to the sighted.

We examined these same measures in the *GUCY2D*-LCA group. At the earliest point of the postretinal visual pathway, the *GUCY2D*-LCA group differed from the comparison blind group. The optic chiasm (Fig. 3A) in *GUCY2D*-LCA subjects did not differ in size from that observed in the sighted ($P = 0.99$), but was significantly larger than seen in the blind ($P = 0.019$), consistent with the preservation of the RGCs and their axonal projections. In comparison, at the level of the visual cortex (Fig. 3E), the *GUCY2D*-LCA group was found to have V1 thickness that was significantly greater than seen in the sighted ($P = 0.0033$) but did not differ from the comparison blind group ($P = 0.21$).

At other points along the visual pathway (LGN volume, pericalcarine volume, and V1 surface area; Figs. 3B–D), measurements in the *GUCY2D*-LCA group were intermediate to those seen in the sighted and comparison blind groups, with nonsignificant differences between the *GUCY2D*-LCA group and either the sighted or comparison blind groups (all P values > 0.091).

Overall, the preservation of axonal input in *GUCY2D*-LCA results in a graded effect upon anatomy. There is preservation of the optic chiasm, intermediate changes through the LGN and pericalcarine white matter, and marked thickening of the visual cortex gray matter typical of severe congenital blindness.

Cross-Modal Responses Within Primary Visual Cortex

In blind populations, nonvisual sensory input produces a response within primary visual cortex. Individual variation in this "cross-modal" response is related to the thickness of V1 cortex[10,28] and to the severity of vision loss.[74] Given the alteration of cortical thickness in the *GUCY2D*-LCA population (Fig. 3E), we would predict that this group should also show cross-modal responses within striate cortex to nonvisual stimuli.

Five of the six *GUCY2D*-LCA patients were studied with BOLD fMRI while they listened to an auditory presentation of sentences played forward and in reverse. The average amplitude of BOLD fMRI response was obtained for these conditions as compared to a white noise stimulus. These data from the *GUCY2D*-LCA group was compared to previously reported data from populations of sighted and blind subjects.[28]

Within primary visual cortex (Fig. 4), different responses were found as a function of group (χ^2 [2 df] = 7.13, $P = 0.028$). Follow-up tests revealed a greater response in the comparison blind group relative to the sighted controls ($P = 0.023$), but no difference between the *GUCY2D*-LCA population and the sighted controls ($P = 0.40$). There was marked variability across the *GUCY2D*-LCA population in the amplitude of cross-modal response. There was perhaps a relation between cross-modal response and visual acuity. The two patients (P3 and P6) with better visual acuity had the smallest cross-modal

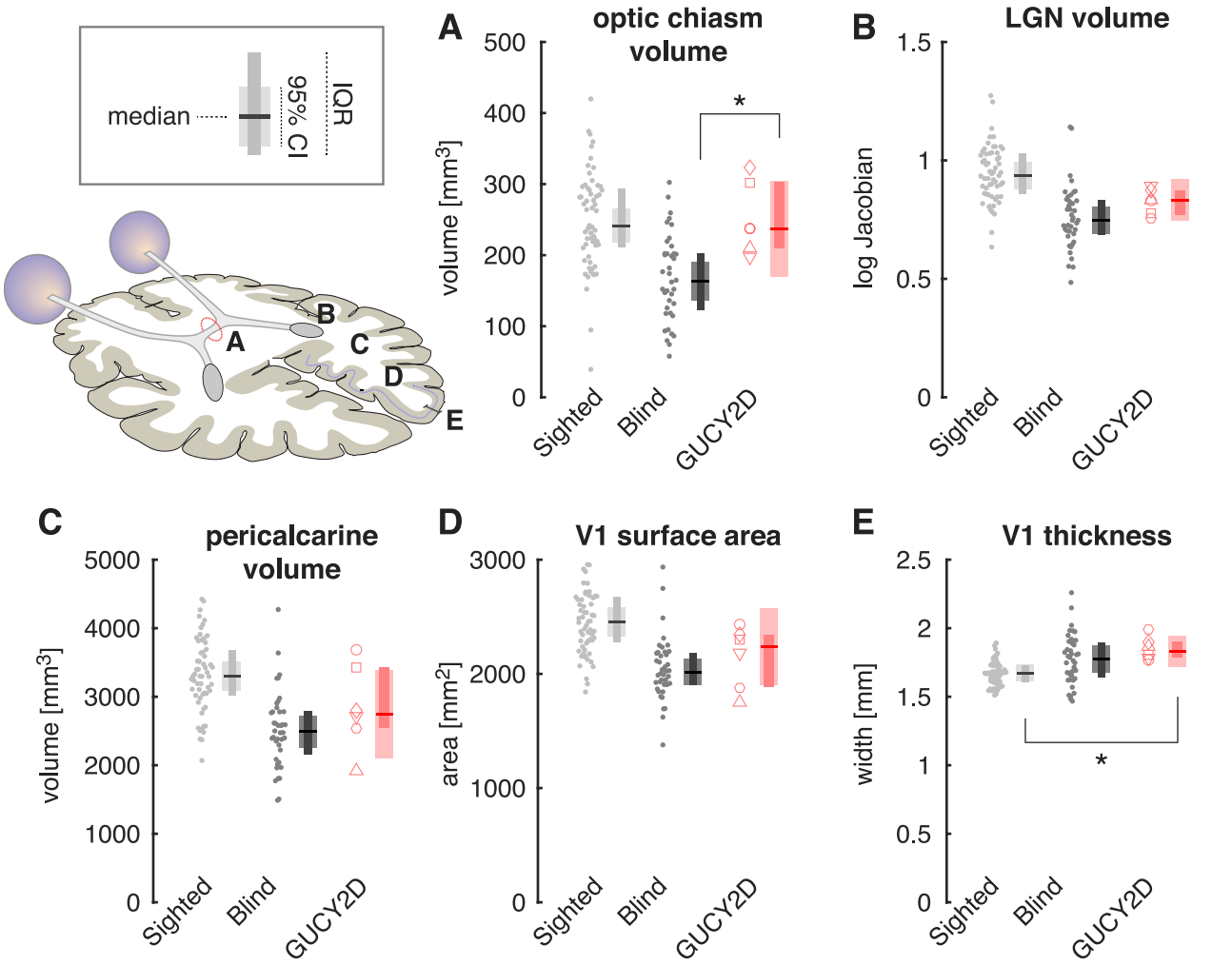

Figure 3. Macroscopic anatomic alterations in *GUCY2D*-LCA. Anatomic measures (illustrated *inset left*) were obtained from T1-weighted, brain MRI scans from the *GUCY2D*-LCA subjects ($n = 6$), as well as previously reported[28] sighted controls ($n = 59$) and participants with congenital blindness of a variety of causes ($n = 40$). Measures were averaged across hemispheres for bilateral structures. Plot points correspond to individual subjects. Plot symbols for the *GUCY2D*-LCA subjects match those used in Figure 1. The summary measure corresponds to the median (*horizontal line*), 95% confidence interval of the median (*thick vertical bar*), and interquartile range (*thin vertical bar*). (**A**) The volume of the optic chiasm; (**B**) the volume of the lateral geniculate nucleus; (**C**) the volume of pericalcarine white matter; (**D**) the surface area of primary visual cortex; (**E**) the thickness of the gray matter layer within primary visual cortex.

responses, while two patients with very poor visual acuity (P1 and P2) had responses that were larger than the response seen in any sighted control.

Altered Resting-State Visual Cortex Activity

The functional organization of visual cortex is also reflected in the correlation of spontaneous neural activity between visual areas.[75–77] These correlations are altered by blindness.[29,30,78–82] A distinctive marker of blindness is a relative increase in the strength of correlations between hierarchically related cortical areas that represent the same quadrant of the visual field (e.g., visual areas V1d and V2d), and a relative decrease in correlations between homotopically related areas that are the different quadrants of given cortical level (e.g., V2v and V2d in the same hemisphere, or V2v in the two hemispheres)[29] (Fig. 5A).

We obtained BOLD fMRI data from the *GUCY2D*-LCA subjects while they rested quietly with their eyes closed in complete darkness. These data were compared to previously reported data in the sighted and congenitally blind.[29,30] The location of the visual areas was determined by reference to an atlas of cortical surface topology.[60] The average BOLD fMRI signal was obtained from each visual area, and the correlation in the signal was measured for pairings of visual areas with hierarchical and homotopic connections. The difference between these measures (hierarchical minus homotopic) was examined for each group (Fig. 5B). In the sighted, stronger correlations are found between homotopically related visual areas as compared to hierarchically related areas. This result is reversed in a general blind population, with stronger correlations between hierarchically related visual areas. The change in the pattern of correlations found in the *GUCY2D*-LCA population matches that seen in other blind people. Nonparametric ANOVA tests confirmed these impressions. The overall effect of group upon the homotopic minus hierarchical correlation values was χ^2 (2 df) = 13.5, $P = 0.0012$. Follow-up tests showed that the comparison blind group differed from the sighted group ($P = 0.0020$), and that the *GUCY2D*-LCA group also differed from the sighted ($P = 0.035$) but not from the blind group ($P = 0.99$).

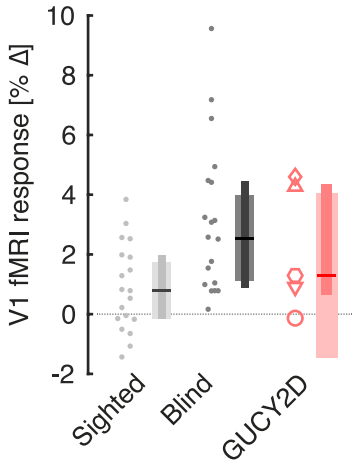

Figure 4. Cross-modal responses within visual cortex. During fMRI scanning, subjects listened to alternating periods of speech (forward and in reverse) and periods of white noise. The cortical response within primary visual cortex to these stimuli was obtained for each subject in the sighted ($n = 19$), blind ($n = 20$), and *GUCY2D*-LCA ($n = 5$) groups. Plot points correspond to individual subjects. Plot symbols for the *GUCY2D*-LCA subjects match those used in Figure 1. The summary measure corresponds to the median (*horizontal line*), 95% confidence interval of the median (*thick vertical bar*), and interquartile range (*thin vertical bar*).

Preservation of White Matter Coherence

We observed earlier that *GUCY2D*-LCA has preserved structural axonal input to the postretinal visual pathway, as evidenced by an intact optic chiasm (Fig. 3A). In a prior study of people with blindness of a variety of causes, we found that the size of the optic chiasm (and the LGN) is associated with postgeniculate white matter coherence in the visual pathway as measured using DTI.[28] We considered if the preservation of chiasmal anatomy in *GUCY2D*-LCA is associated with normal measures of white matter organization along the postgeniculate pathway, despite the severe and lifelong visual impairment caused by this disease.

We obtained DTI measures of whole-brain FA from the *GUCY2D*-LCA group. These measures were compared with previously reported data obtained from sighted subjects and the comparison blind group.[28] When FA maps are averaged across individuals within each group (Fig. 6A) there is an appreciable difference in FA values along the optic radiations in the sighted and the blind. In contrast, the *GUCY2D*-LCA group has normal-appearing FA values. We quantified these impressions by obtaining the FA within the optic radiations and splenium of the corpus callosum in each subject (Fig. 6B). There was a significant effect of group on the measure (χ^2 [2 df] = 12.1, $P = 0.0023$). Follow-up tests revealed that, while there was not a difference in FA values in the postgeniculate pathway between the *GUCY2D*-LCA group and the sighted ($P = 0.35$), the comparison blind group had significantly lower FA values as compared to the *GUCY2D*-LCA subjects ($P = 0.0067$), confirming the impression that blindness from *GUCY2D*-LCA does not result in an alteration of white matter organization for this measure of DTI.

Our measure of FA was from a ROI that combined the splenium of the corpus callosum and the optic radiations. The combination of these measures was motivated by both their shared developmental trajectory[83,84] and the anatomic intermingling of the forceps major of the splenium and the optic radiations. We nonetheless confirmed that these same findings are present in separate ROIs that define the optic radiations (FA of optic radiations, sighted versus *GUCY2D*-LCA: $P = 0.38$; comparison blind group versus *GUCY2D*-LCA: $P = 0.0038$) and splenium (FA of splenium, sighted versus *GUCY2D*-LCA: $P = 0.54$; comparison blind group versus *GUCY2D*-LCA: $P =$

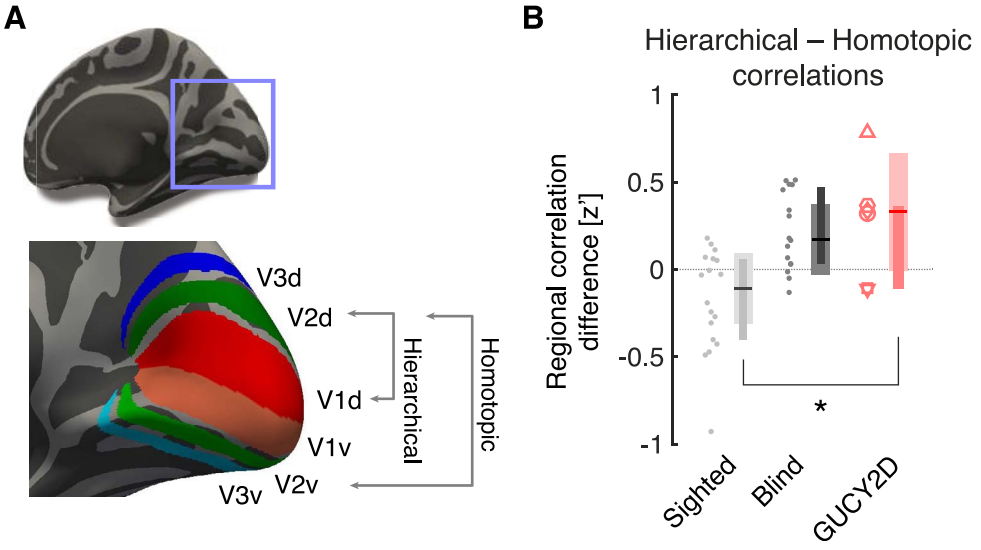

Figure 5. Correlation of spontaneous signals in visual cortex. (**A**) There are six quarter-area cortical representations in each brain hemisphere, corresponding to the dorsal and ventral aspects of visual areas V1, V2, and V3. BOLD fMRI data were collected from participants while they rested with eyes closed in darkness. The correlation in the BOLD fMRI signal between each pairing of cortical visual areas was obtained for each subject. Some pairings have a hierarchical relationship, in that they are sequential areas in the visual hierarchy that represent the same quarter field. Some pairings are homotopic, in that they are different quarter-field representations at the same level of the visual hierarchy. (**B**) The difference in correlation (expressed as a Fischer z′) for hierarchical and homotopic regional pairings was obtained for each subject in the sighted ($n = 18$), blind ($n = 21$), and *GUCY2D*-LCA groups ($n = 6$). Plot points correspond to individual subjects. Plot symbols for the *GUCY2D*-LCA subjects match those used in Figure 1. The summary measure corresponds to the median (*horizontal line*), 95% confidence interval of the median (*thick vertical bar*), and interquartile range (*thin vertical bar*).

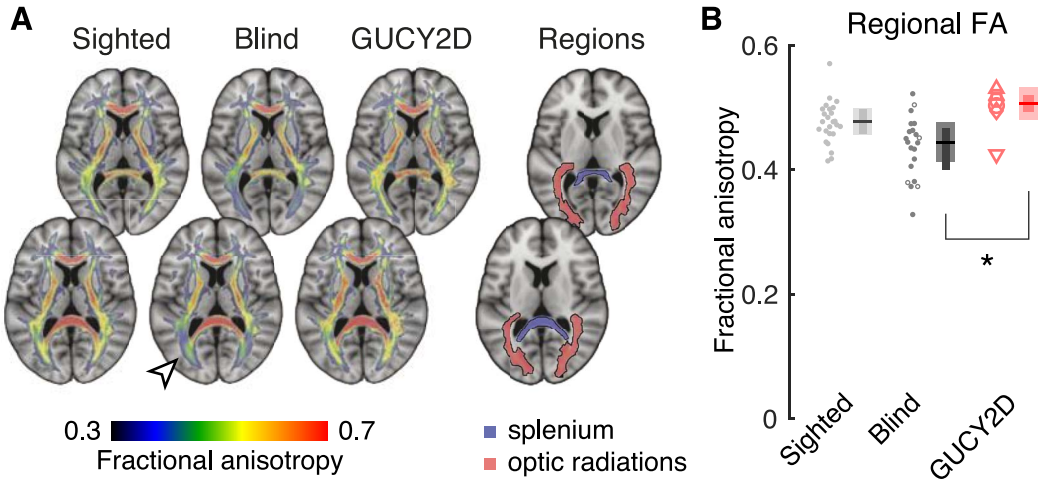

Figure 6. White matter coherence along the visual pathway. (**A**) Fractional anisotropy (FA) was measured using whole-brain diffusion tensor imaging for each subject. The average FA map for the sighted ($n = 25$), comparison blind ($n = 21$), and *GUCY2D*-LCA ($n = 6$) groups is shown at two axial slices. The locations of the optic radiations and splenium of the corpus callosum are indicated. (**B**) The average FA value within the optic radiations and splenium was obtained for each subject. Plot points correspond to individual subjects. *Open gray circles* indicate those subjects with congenital blindness for whom glaucoma contributed to their vision loss. Plot symbols for the *GUCY2D*-LCA subjects match those used in Figure 1. The summary measure corresponds to the median (*horizontal line*), 95% confidence interval of the median (*thick vertical bar*), and interquartile range (*thin vertical bar*). A reduction in FA values along the postgeniculate visual pathway is seen for the blind as compared to the sighted. In contrast to other blind participants, the *GUCY2D*-LCA group has a normal FA value.

0.031). Some of the subjects in the sighted and comparison blind groups were studied with a slightly different DTI protocol, which we have previously shown produces the same measurement within the postgeniculate pathway.[28] We repeated the analysis using only those sighted and comparison blind subjects who were studied with the identical DTI protocol as used with the *GUCY2D*-LCA population. We obtained the same results (FA of optic radiations, matched DTI protocols, sighted versus *GUCY2D*-LCA: $P = 0.59$; comparison blind group versus *GUCY2D*-LCA: $P = 0.0060$).

Subject age is associated with a small, linear reduction in global brain FA values, although this effect is minimal within the occipital lobes.[85] We examined in our data if modeling the small differences in age between the studied groups could account for our group effects. The linear effect of subject age was regressed from the FA measures and the comparisons were repeated. We obtained the same results (FA of optic radiations, matched DTI protocols, linear age effects removed, sighted versus *GUCY2D*-LCA: $P = 0.21$; comparison blind group versus *GUCY2D*-LCA: $P = 0.0097$).

Four of the subjects in the comparison blind group had congenital glaucoma as a contributing factor in their vision loss. As glaucoma is particularly damaging to axons of the RGCs, we tested if the FA difference between the comparison blind group and the GUCY2D-LCA group would persist after excluding these subjects. This was the case (FA of optic radiations, matched DTI protocols, linear age effects removed, excluding congenital glaucoma subjects: comparison blind group versus *GUCY2D*-LCA: $P = 0.010$).

Discussion

We find that the dissociation of retinal structure and function in *GUCY2D*-LCA is reflected within the postretinal pathways of the brain. Patients with *GUCY2D*-LCA have a profound, or complete, congenital impairment in cone function, with associated nystagmus and severe functional visual impairments.[24] Correspondingly, cortical responses to light stimulation are attenuated and restricted. This visual impairment is accompanied by thickening of the gray matter layer of the visual cortex and functional alterations of the occipital lobe, including changes in resting-state activity. In these measures, the *GUCY2D*-LCA group does not differ from a population of congenitally blind subjects with destructive lesions of the retina. In marked contrast, the structure of the retina as assessed by OCT is nearly normal. This preservation of retinal architecture is reflected in the normal size of the optic chiasm, and is associated with normal postgeniculate white matter organization as measured with DTI. These results suggest that dissociable properties of retinal anatomy and function shape the visual pathways of the brain.

The Role of the Retinal Ganglion Cells

In addition to a reduction in the overall size of the optic radiations,[1–3] studies of people with congenital blindness have consistently found a reduction in FA within the postgeniculate pathway.[4,5,86] We obtain this result as well in our group of people with severe congenital blindness from damage to the retina. In comparison, we find that measures of FA within the optic radiations are normal in *GUCY2D*-LCA. We cannot explain our results on the basis of subject age, technical aspects of data acquisition, or the precise region of the postgeniculate pathway that is interrogated.

Our findings in *GUCY2D*-LCA do not seem to be a feature of all forms of retinal degeneration. Ogawa and colleagues[19] found reductions in FA along the optic radiations in five patients with adult-onset, cone–rod dystrophy (genotype not reported). Similarly, a reduction in FA within the optic radiations has been reported in the RPE65 (retinal pigment epithelium-specific protein 65 kDa) subtype of LCA.[87]

GUCY2D-LCA differs from both of these forms of retinal degeneration in having relatively preserved anatomy of the neural retina in the presence of marked photoreceptor dysfunction.[24] *RPE65*-LCA has a more complicated relationship between photoreceptor dysfunction and retinal degeneration.[35,88,89] While there can be patches of retina with

preserved structure in the face of impaired function, there is considerable degeneration at other retinal sites at all stages of the disease.

The preservation of white matter pathways in *GUCY2D*-LCA may be related to the maintained trophic influence of the RGCs, thus preventing the anterograde, transynaptic degeneration along the visual pathway that has long been recognized to occur after loss of axons arising from the retina.[17,90,91]

Ogawa and colleagues[19] used fiber tractography to isolate the optic radiations and measure FA as a function of position along the length of this white matter tract. We did not pursue this type of analysis, as we were chiefly motivated to obtain a single, highly reliable measure given the amount of DTI data available as part of this multimodal study. It is possible that our finding of no difference in FA between the *GUCY2D*-LCA group and the sighted masks a subtle, local difference in FA that would be revealed by such an analysis. We note, however, that Ogawa and colleagues found a roughly uniform reduction in FA along the length of the optic radiations in the cone–rod dystrophy population, and that there is no particular reason to suspect that *GUCY2D*-LCA would alter white matter properties at a particular point along the optic radiations.

Form Vision and Cortical Development

While a preserved RGC layer is a prominent feature of *GUCY2D*-LCA, studies in animals suggest that this is not sufficient to maintain a normal postretinal visual pathway. Animal models employ postnatal lid suture or dark rearing to deprive the developing visual system of the neural responses to formed visual input while retaining the anatomic integrity of the retina. Across species, these interventions produce atrophy of the LGN and its neural cell bodies.[17,91–93] Therefore, while anatomic preservation of the RGCs is crucial, retinal function also contributes to preservation of the visual pathway.

Loss of functional input is presumably responsible for the changes in postretinal structure and function that we observe in *GUCY2D*-LCA. Despite the presence of a normal optic chiasm and postgeniculate white matter anisotropy, *GUCY2D*-LCA patients have a thickened striate gray matter layer. The degree of cortical thickening found in blind people is proportional to the timing[94] and severity of vision loss.[74] The *GUCY2D*-LCA population has somewhat better residual visual function than the comparison blind group. It is possible that this difference contributes to the differences in brain measures we observe between the groups, independent of the preservation of the RGCs per se. We note, however, that V1 cortical thickness in *GUCY2D*-LCA was at least equal to that observed in the congenitally blind subjects. This indicates that both groups experienced early and severe form vision deprivation, despite the differences in residual visual perception in adulthood.

Early synaptic remodeling in response to formed visual input shapes visual cortex,[8,14] and has been proposed as the mechanism that produces cortical thinning with development.[6] The alterations we find in striate cortex in *GUCY2D*-LCA confirm that the neural response to formed visual input plays an instructive role in the shaping of human visual cortex, and that simple anatomic preservation of the retinogeniculate pathway is not sufficient for normal cortical maturation.

Cross-modal responses within visual areas may reflect retention of diffuse synaptic connections in immature cortex. We found variable cross-modal responses across the *GUCY2D*-LCA patients to auditory stimulation. More definitive was the alteration of the pattern of spontaneous occipital cortex activity, similar to what is found in other causes of congenital blindness. Therefore, despite the maintenance of structural aspects of the visual pathway, the profound photoreceptor disruption produced by *GUCY2D* mutations leads to a visual cortex that reflects a lifetime of severe deprivation of form vision.

It is possible that these changes to the postchiasmatic pathway in *GUCY2D*-LCA occur not only in the presence of a structurally intact retina, but accompanied by ongoing retinal activity as well. In the *rd1* mouse, normal retinal waves occur within the RGCs during prenatal development. In the postnatal period, as the rods and cones degenerate, an abnormal pattern of hyperactivity develops.[95] In the adult *rd1* mouse, this hyperactivity has the form of ongoing oscillatory (~10 Hz) firing in the RGCs.[96] In another model of retinal degeneration (the $Crx^{-/-}$ mouse) bipolar cells become uncoupled from photoreceptors, and again rhythmic RGC hyperactivity is seen at the time of eye opening (in this case at ~5 Hz).[97] Rhythmic RGC activity is known to reach postretinal neural sites (reviewed in Ref. 98), and these animals are found to have preserved eye-specific LGN laminar organization.[97] This is in contrast to the atrophy and regression of LGN laminar organization that follows interruption of retinal activity by pharmacologic intervention[99] or dark rearing.[93,100,101]

These findings in animal models of inherited retinal disease raise the possibility that spontaneous neural activity is present within the RGCs of *GUCY2D*-LCA. If present, such activity might contribute to the preservation of white matter pathways that we observe. More generally, how spontaneous activity in rodent models of retinal degeneration relates to specific forms of retinal disease in humans, and further to the organization of the postretinal pathway, is yet to be explored.

Prospects for Vision Restoration

Successful targeting of the residual but dysfunctional photoreceptors (and retinal pigment epithelium) using gene augmentation therapy has prompted consideration of a similar therapeutic approach for *GUCY2D*-LCA.[21,22,102] In the rodent, gene therapy of a homologous guanylate cyclase-1 mutation has been shown to improve function and visual behavior.[103–106]

Recovery of visual function is limited both by ocular treatment and by receptivity of the postretinal pathway for restored visual input. Treatment of people with longstanding anterior segment disease has provided conflicting outcomes. Patient MM regained monocular vision after treatment of corneal scaring that had been present between the ages of 3 and 46. Following surgery, he regained normal contrast sensitivity for low spatial frequency stimuli.[107] However, even 10 years after recovery, his spatial acuity and object recognition were little improved.[108] In contrast, children with bilateral congenital cataracts who receive treatment between the ages of 8 and 17 have steady improvements in spatial acuity in the months following surgery.[20]

It is unclear how these outcomes relate to the treatment of LCA. Inherited photoreceptor dysfunction may provide the developing visual system with a quite different set of functional inputs. Unlike the treatment of anterior segment disease, retinal gene therapy in *RPE65*-LCA produces a focal area of treated retina that continues to degenerate along with surrounding abnormal, untreated photoreceptors.[88,109] In those patients with *RPE65*-LCA who have undergone successful therapy, the treated regions of retina have improved luminance sensitivity.[109–111] In some cases, patients come to use the treated area of retina as an extrafoveal locus for fixation.[32,112] This use of a pseudo-fovea arises many months after the initial improvement in luminance sensitivity.[32,112] suggesting a slow alteration of cortical visual processing and control of eye movements.

Investigative Ophthalmology & Visual Science

There are limited data to guide how pretreatment measures of the brain relate to recovery of visual function. In the case of patient MM, his impaired visual perception was accompanied by persistent abnormalities in the diffusion tensor properties of his optic radiations 7 years after treatment,[86] although there is reportedly a normalization of DTI measures in *RPE65*-LCA after gene therapy,[87] accompanied by an increase fMRI responses in visual cortex to light stimulation.[113] We therefore regard our finding of preserved white matter coherence of the postretinal pathway to be a promising sign for recovery in *GUCY2D*-LCA. It remains to be seen if the independent alterations in cortical thickness and spontaneous neural activity that are present in blindness present an impediment to recovered vision.

Acknowledgments

Supported by National Institutes of Health Grants R01 EY020516 (GKA), P30 EY001583 (Core Grant for Vision Research), P30 NS045839 (Neuroscience Neuroimaging Center Core Grant), and by grants from the Foundation Fighting Blindness, Macula Vision Research Foundation, Hope for Vision, and the Research to Prevent Blindness. The authors alone are responsible for the content and writing of the paper.

Disclosure: **G.K. Aguirre**, None; **O.H. Butt**, None; **R. Datta**, None; **A.J. Roman**, None; **A. Sumaroka**, None; **S.B. Schwartz**, None; **A.V. Cideciyan**, None; **S.G. Jacobson**, None

References

1. Noppeney U, Friston KJ, Ashburner J, Frackowiak R, Price CJ. Early visual deprivation induces structural plasticity in gray and white matter. *Curr Biol*. 2005;15:R488–R490.
2. Pan WJ, Wu G, Li CX, Lin F, Sun J, Lei H. Progressive atrophy in the optic pathway and visual cortex of early blind Chinese adults: a voxel-based morphometry magnetic resonance imaging study. *Neuroimage*. 2007;37:212–220.
3. Ptito M, Schneider FC, Paulson OB, Kupers R. Alterations of the visual pathways in congenital blindness. *Exp Brain Res*. 2008;187:41–49.
4. Bridge H, Cowey A, Ragge N, Watkins K. Imaging studies in congenital anophthalmia reveal preservation of brain architecture in "visual" cortex. *Brain*. 2009;132:3467–3480.
5. Shimony J, Burton H, Epstein A, McLaren D, Sun S, Snyder A. Diffusion tensor imaging reveals white matter reorganization in early blind humans. *Cereb Cortex*. 2006;16:1653–1661.
6. Jiang J, Zhu W, Shi F, et al. Thick visual cortex in the early blind. *J Neurosci*. 2009;29:2205–2211.
7. Park HJ, Lee JD, Kim EY, et al. Morphological alterations in the congenital blind based on the analysis of cortical thickness and surface area. *Neuroimage*. 2009;47:98–106.
8. Bourgeois JP, Jastreboff PJ, Rakic P. Synaptogenesis in visual cortex of normal and preterm monkeys: evidence for intrinsic regulation of synaptic overproduction. *Proc Natl Acad Sci U S A*. 1989;86:4297–4301.
9. Stryker MP, Harris WA. Binocular impulse blockade prevents the formation of ocular dominance columns in cat visual cortex. *J Neurosci*. 1986;6:2117–2133.
10. Anurova I, Renier LA, De Volder AG, Carlson S, Rauschecker JP. Relationship between cortical thickness and functional activation in the early blind. *Cereb Cortex*. 2014;25:2035–2048.
11. Bedny M, Pascual-Leone A, Dodell-Feder D, Fedorenko E, Saxe R. Language processing in the occipital cortex of congenitally blind adults. *Proc Natl Acad Sci U S A*. 2011;108:4429–4434.
12. Sadato N, Pascual-Leone A, Grafman J, et al. Activation of the primary visual cortex by Braille reading in blind subjects. *Nature*. 1996;380:526–528.
13. Coogan TA, Van Essen DC. Development of connections within and between areas V1 and V2 of macaque monkeys. *J Comp Neurol*. 1996;372:327–342.
14. Innocenti GM, Price DJ. Exuberance in the development of cortical networks. *Nat Rev Neurosci*. 2005;6:955–965.
15. Ackman JB, Burbridge TJ, Crair MC. Retinal waves coordinate patterned activity throughout the developing visual system. *Nature*. 2012;490:219–225.
16. McAllister AK, Katz LC, Lo DC. Neurotrophins and synaptic plasticity. *Annu Rev Neurosci*. 1999;22:295–318.
17. Kalil R. A quantitative study of the effects of monocular enucleation and deprivation on cell growth in the dorsal lateral geniculate nucleus of the cat. *J Comp Neurol*. 1980;189:483–524.
18. Riddle DR, Lo DC, Katz LC. NT-4-mediated rescue of lateral geniculate neurons from effects of monocular deprivation. *Nature*. 1995;378:189–191.
19. Ogawa S, Takemura H, Horiguchi H, et al. White matter consequences of retinal receptor and ganglion cell damage. *Invest Ophthalmol Vis Sci*. 2014;55:6976–6986.
20. Kalia A, Lesmes LA, Dorr M, et al. Development of pattern vision following early and extended blindness. *Proc Natl Acad Sci U S A*. 2014;111:2035–2039.
21. Boye SE, Boye SL, Lewin AS, Hauswirth WW. A comprehensive review of retinal gene therapy. *Mol Ther*. 2013;21:509–519.
22. Cideciyan AV. Leber congenital amaurosis due to RPE65 mutations and its treatment with gene therapy. *Prog Retin Eye Res*. 2010;29:398–427.
23. den Hollander AI, Roepman R, Koenekoop RK, Cremers FP. Leber congenital amaurosis: genes, proteins and disease mechanisms. *Prog Retin Eye Res*. 2008;27:391–419.
24. Jacobson SG, Cideciyan AV, Peshenko IV, et al. Determining consequences of retinal membrane guanylyl cyclase (RetGC1) deficiency in human Leber congenital amaurosis en route to therapy: residual cone-photoreceptor vision correlates with biochemical properties of the mutants. *Hum Mol Genet*. 2013;22:168–183.
25. Walia S, Fishman GA, Jacobson SG, et al. Visual acuity in patients with Leber's congenital amaurosis and early childhood-onset retinitis pigmentosa. *Ophthalmology*. 2010;117:1190–1198.
26. Pasadhika S, Fishman GA, Stone EM, et al. Differential macular morphology in patients with RPE65-, CEP290-, GUCY2D-, and AIPL1-related Leber congenital amaurosis. *Invest Ophthalmol Vis Sci*. 2010;51:2608–2614.
27. Aguirre GK, Komaromy AM, Cideciyan AV, et al. Canine and human visual cortex intact and responsive despite early retinal blindness from RPE65 mutation. *PLoS Med*. 2007;4:e230.
28. Aguirre GK, Datta R, Benson N, et al. Patterns of individual variation in visual pathway structure and function in the sighted and blind. *PLoS One*. 2016;11:e0164677.
29. Butt OH, Benson NC, Datta R, Aguirre GK. Hierarchical and homotopic correlations of spontaneous neural activity within the visual cortex of the sighted and blind. *Front Hum Neurosci*. 2014;9:25.
30. Butt OH, Benson NC, Datta R, Aguirre GK. The fine-scale functional correlation of striate cortex in sighted and blind people. *J Neurosci*. 2013;33:16209–16219.
31. Cideciyan AV, Aleman TS, Jacobson SG, et al. Centrosomal-ciliary gene CEP290/NPHP6 mutations result in blindness with unexpected sparing of photoreceptors and visual brain: implications for therapy of Leber congenital amaurosis. *Hum Mutat*. 2007;28:1074–1083.

32. Cideciyan AV, Aguirre GK, Jacobson SG, et al. Pseudo-fovea formation after gene therapy for RPE65-LCA. *Invest Ophthalmol Vis Sci*. 2015;56:526–537.
33. Jacobson SG, Cideciyan AV, Aleman TS, et al. Crumbs homolog 1 (CRB1) mutations result in a thick human retina with abnormal lamination. *Hum Mol Genet*. 2003;12:1073–1078.
34. Jacobson S, Sumaroka A, Luo X, Cideciyan A. Retinal optogenetic therapies: clinical criteria for candidacy. *Clin Genet*. 2013;84:175–182.
35. Jacobson SG, Aleman TS, Cideciyan AV, et al. Identifying photoreceptors in blind eyes caused by RPE65 mutations: prerequisite for human gene therapy success. *Proc Natl Acad Sci U S A*. 2005;102:6177–6182.
36. Aleman TS, Cideciyan AV, Sumaroka A, et al. Retinal laminar architecture in human retinitis pigmentosa caused by Rhodopsin gene mutations. *Invest Ophthalmol Vis Sci*. 2008;49:1580–1590.
37. Aleman TS, Soumittra N, Cideciyan AV, et al. CERKL mutations cause an autosomal recessive cone-rod dystrophy with inner retinopathy. *Invest Ophthalmol Vis Sci*. 2009;50:5944–5954.
38. Jacobson SG, Aleman TS, Sumaroka A, et al. Disease boundaries in the retina of patients with Usher syndrome caused by MYO7A gene mutations. *Invest Ophthalmol Vis Sci*. 2009;50:1886–1894.
39. Sakami S, Maeda T, Bereta G, et al. Probing mechanisms of photoreceptor degeneration in a new mouse model of the common form of autosomal dominant retinitis pigmentosa due to P23H opsin mutations. *J Biol Chem*. 2011;286:10551–10567.
40. Huang Y, Cideciyan AV, Papastergiou GI, et al. Relation of optical coherence tomography to microanatomy in normal and rd chickens. *Invest Ophthalmol Vis Sci*. 1998;39:2405–2416.
41. Spaide RF, Curcio CA. Anatomical correlates to the bands seen in the outer retina by optical coherence tomography: literature review and model. *Retina*. 2011;31:1609–1619.
42. Sadigh S, Luo X, Cideciyan AV, et al. Drusen and photoreceptor abnormalities in African-Americans with intermediate non-neovascular age-related macular degeneration. *Curr Eye Res*. 2015;40:398–406.
43. Lujan BJ, Roorda A, Knighton RW, Carroll J. Revealing Henle's fiber layer using spectral domain optical coherence tomography. *Invest Ophthalmol Vis Sci*. 2011;52:1486–1492.
44. Tong KK, Lujan BJ, Zhou Y, Lin MC. Directional optical coherence tomography reveals reliable outer nuclear layer measurements. *Optom Vis Sci*. 2016;93:714–719.
45. Dale AM, Fischl B, Sereno MI. Cortical surface-based analysis: I. Segmentation and surface reconstruction. *Neuroimage*. 1999;9:179–194.
46. Fischl B, Sereno MI, Dale AM. Cortical surface-based analysis: II: inflation, flattening, and a surface-based coordinate system. *Neuroimage*. 1999;9:195–207.
47. Fischl B, Sereno MI, Tootell RB, et al. High-resolution intersubject averaging and a coordinate system for the cortical surface. *Hum Brain Mapp*. 1999;8:272–284.
48. Fischl B, Dale AM. Measuring the thickness of the human cerebral cortex from magnetic resonance images. *Proc Natl Acad Sci U S A*. 2000;97:11050–11055.
49. Segonne F, Dale A, Busa E, et al. A hybrid approach to the skull stripping problem in MRI. *Neuroimage*. 2004;22:1060–1075.
50. Fischl B, van der Kouwe A, Destrieux C, et al. Automatically parcellating the human cerebral cortex. *Cereb Cortex*. 2004;14:11–22.
51. Fischl B, Salat DH, Busa E, et al. Whole brain segmentation: automated labeling of neuroanatomical structures in the human brain. *Neuron*. 2002;33:341–355.
52. Sled JG, Zijdenbos AP, Evans AC. A nonparametric method for automatic correction of intensity nonuniformity in MRI data. *IEEE Trans Med Imaging*. 1998;17:87–97.
53. Dale AM, Sereno MI. Improved localization of cortical activity by combining EEG and MEG with MRI cortical surface reconstruction: a linear approach. *J Cogn Neurosci*. 1993;5:162–176.
54. Fischl B, Liu A, Dale AM. Automated manifold surgery: constructing geometrically accurate and topologically correct models of the human cerebral cortex. *IEEE Trans Med Imaging*. 2001;20:70–80.
55. Ségonne F, Pacheco J, Fischl B. Geometrically accurate topology-correction of cortical surfaces using nonseparating loops. *IEEE Trans Med Imaging*. 2007;26:518–529.
56. Bürgel U, Schormann T, Schleicher A, Zilles K. Mapping of histologically identified long fiber tracts in human cerebral hemispheres to the MRI volume of a reference brain: position and spatial variability of the optic radiation. *Neuroimage*. 1999;10:489–499.
57. Bürgel U, Amunts K, Hoemke L, Mohlberg H, Gilsbach JM, Zilles K. White matter fiber tracts of the human brain: three-dimensional mapping at microscopic resolution, topography and intersubject variability. *Neuroimage*. 2006;29:1092–1105.
58. Eickhoff SB, Stephan KE, Mohlberg H, et al. A new SPM toolbox for combining probabilistic cytoarchitectonic maps and functional imaging data. *Neuroimage*. 2005;25:1325–1335.
59. Destrieux C, Fischl B, Dale A, Halgren E. Automatic parcellation of human cortical gyri and sulci using standard anatomical nomenclature. *Neuroimage*. 2010;53:1–15.
60. Benson NC, Butt OH, Brainard DH, Aguirre GK. Correction of distortion in flattened representations of the cortical surface allows prediction of V1-V3 functional organization from anatomy. *PLoS Comput Biol*. 2014;10:e1003538.
61. Benson NC, Butt OH, Datta R, Radoeva PD, Brainard DH, Aguirre GK. The retinotopic organization of striate cortex is well predicted by surface topology. *Curr Biol*. 2012;22:2081–2085.
62. Hinds OP, Rajendran N, Polimeni JR, et al. Accurate prediction of V1 location from cortical folds in a surface coordinate system. *Neuroimage*. 2008;39:1585–1599.
63. Avants B, Gee JC. Geodesic estimation for large deformation anatomical shape averaging and interpolation. *Neuroimage*. 2004;23:S139–S150.
64. Mazziotta JC, Toga AW, Evans A, Fox P, Lancaster J. A probabilistic atlas of the human brain: theory and rationale for its development. The International Consortium for Brain Mapping (ICBM). *Neuroimage*. 1995;2:89–101.
65. Basser PJ, Mattiello J, LeBihan D. MR diffusion tensor spectroscopy and imaging. *Biophys J*. 1994;66:259–267.
66. Hua K, Zhang J, Wakana S, et al. Tract probability maps in stereotaxic spaces: analyses of white matter anatomy and tract-specific quantification. *Neuroimage*. 2008;39:336–347.
67. Wakana S, Caprihan A, Panzenboeck MM, et al. Reproducibility of quantitative tractography methods applied to cerebral white matter. *Neuroimage*. 2007;36:630–644.
68. Aguirre GK, Zarahn E, D'esposito M. The variability of human, BOLD hemodynamic responses. *Neuroimage*. 1998;8:360–369.
69. Greve DN, Van der Haegen L, Cai Q, et al. A surface-based analysis of language lateralization and cortical asymmetry. *J Cogn Neurosci*. 2013;25:1477–1492.

Investigative Ophthalmology & Visual Science

70. Biswal B, Yetkin F, Haughton VM, Hyde JS. Functional connectivity in the motor cortex of resting human brain using echo-planar MRI. *Magn Reson Med*. 1995;34:537–541.
71. Yeo BT, Krienen FM, Sepulcre J, et al. The organization of the human cerebral cortex estimated by intrinsic functional connectivity. *J Neurophysiol*. 2011;106:1125–1165.
72. Sjöstrand J, Popovic Z, Conradi N, Marshall J. Morphometric study of the displacement of retinal ganglion cells subserving cones within the human fovea. *Graefes Arch Clin Exp Ophthalmol*. 1999;237:1014–1023.
73. Cecchetti L, Ricciardi E, Handjaras G, Kupers R, Ptito M, Pietrini P. Congenital blindness affects diencephalic but not mesencephalic structures in the human brain. *Brain Struct Funct*. 2016;221:1465–1480.
74. Cunningham SI, Weiland JD, Bao P, Lopez-Jaime GR, Tjan BS. Correlation of vision loss with tactile-evoked V1 responses in retinitis pigmentosa. *Vision Res*. 2015;111:197–207.
75. Arcaro MJ, Honey CJ, Mruczek RE, Kastner S, Hasson U. Widespread correlation patterns of fMRI signal across visual cortex reflect eccentricity organization. *Elife*. 2015;4:e03952.
76. Heinzle J, Kahnt T, Haynes JD. Topographically specific functional connectivity between visual field maps in the human brain. *Neuroimage*. 2011;56:1426–1436.
77. Raemaekers M, Schellekens W, van Wezel RJ, Petridou N, Kristo G, Ramsey NF. Patterns of resting state connectivity in human primary visual cortical areas: a 7T fMRI study. *Neuroimage*. 2014;84:911–921.
78. Liu Y, Yu C, Liang M, et al. Whole brain functional connectivity in the early blind. *Brain*. 2007;130:2085–2096.
79. Yu C, Liu Y, Li J, et al. Altered functional connectivity of primary visual cortex in early blindness. *Hum Brain Mapp*. 2008;29:533–543.
80. Watkins KE, Cowey A, Alexander I, et al. Language networks in anophthalmia: maintained hierarchy of processing in "visual" cortex. *Brain*. 2012;135:1566–1577.
81. Burton H, Snyder AZ, Raichle ME. Resting state functional connectivity in early blind humans. *Front Syst Neurosci*. 2014;8:51.
82. Bock AS, Binda P, Benson NC, Bridge H, Watkins KE, Fine I. Resting-state retinotopic organization in the absence of retinal input and visual experience. *J Neurosci*. 2015;35:12366–12382.
83. Lund R, Mustari M. Development of the geniculocortical pathway in rat. *J Comp Neurol*. 1977;173:289–305.
84. Olavarria J, van Sluyters RC. Organization and postnatal development of callosal connections in the visual cortex of the rat. *J Comp Neurol*. 1985;239:1–26.
85. Salat D, Tuch D, Greve D, et al. Age-related alterations in white matter microstructure measured by diffusion tensor imaging. *Neurobiol Aging*. 2005;26:1215–1227.
86. Levin N, Dumoulin SO, Winawer J, Dougherty RF, Wandell BA. Cortical maps and white matter tracts following long period of visual deprivation and retinal image restoration. *Neuron*. 2010;65:21–31.
87. Ashtari M, Zhang H, Cook PA, et al. Plasticity of the human visual system after retinal gene therapy in patients with Leber's congenital amaurosis. *Sci Transl Med*. 2015;7:296ra110.
88. Cideciyan AV, Jacobson SG, Beltran WA, et al. Human retinal gene therapy for Leber congenital amaurosis shows advancing retinal degeneration despite enduring visual improvement. *Proc Natl Acad Sci U S A*. 2013;110:E517–E525.
89. Jacobson SG, Cideciyan AV, Aleman TS, et al. Photoreceptor layer topography in children with leber congenital amaurosis caused by RPE65 mutations. *Invest Ophthalmol Vis Sci*. 2008;49:4573–4577.
90. Colombo M, Colombo A, Gross CG. Panizza's Bartolomeo "Observations on the optic nerve" (1855). *Brain Res Bull*. 2002;58:529–539.
91. Chow KL, Spear PD. Morphological and functional effects of visual deprivation on the rabbit visual system. *Exp Neurol*. 1974;42:429–447.
92. Crawford M, Pesch T, Von Noorden G, Harwerth R, Smith E. Bilateral form deprivation in monkeys. Electrophysiologic and anatomic consequences. *Invest Ophthalmol Vis Sci*. 1991;32:2328–2336.
93. Jameie S, Abdolrahmani M, Nobakht M, et al. Effects of total light deprivation on dorsal lateral geniculate nucleus of male neonate rats. *Oman Med J*. 2010;25:179–183.
94. Li Q, Song M, Xu J, Qin W, Yu C, Jiang T. Cortical thickness development of human primary visual cortex related to the age of blindness onset [published online ahead of print July 28, 2016]. *Brain Imaging Behav*. doi: 10.1007/s11682-016-9576-8.
95. Stasheff SF. Emergence of sustained spontaneous hyperactivity and temporary preservation of OFF responses in ganglion cells of the retinal degeneration (rd1) mouse. *J Neurophysiol*. 2008;99:1408–1421.
96. Margolis DJ, Newkirk G, Euler T, Detwiler PB. Functional stability of retinal ganglion cells after degeneration-induced changes in synaptic input. *J Neurosci*. 2008;28:6526–6536.
97. Soto F, Ma X, Cecil JL, Vo BQ, Culican SM, Kerschensteiner D. Spontaneous activity promotes synapse formation in a cell-type-dependent manner in the developing retina. *J Neurosci*. 2012;32:5426–5439.
98. Trenholm S, Awatramani GB. Origins of spontaneous activity in the degenerating retina. *Front Cell Neurosci*. 2015;9:277.
99. Chapman B. Necessity for afferent activity to maintain eye-specific segregation in ferret lateral geniculate nucleus. *Science*. 2000;287:2479–2482.
100. Demas J, Eglen SJ, Wong RO. Developmental loss of synchronous spontaneous activity in the mouse retina is independent of visual experience. *J Neurosci*. 2003;23:2851–2860.
101. Tian N, Copenhagen DR. Visual deprivation alters development of synaptic function in inner retina after eye opening. *Neuron*. 2001;32:439–449.
102. Boye SE. Leber congenital amaurosis caused by mutations in GUCY2D. *Cold Spring Harb Perspect Med*. 2014;5:a017350.
103. Boye SL, Conlon T, Erger K, et al. Long-term preservation of cone photoreceptors and restoration of cone function by gene therapy in the guanylate cyclase-1 knockout (GC1KO) mouse. *Invest Ophthalmol Vis Sci*. 2011;52:7098–7108.
104. Boye SE, Boye SL, Pang J, et al. Functional and behavioral restoration of vision by gene therapy in the guanylate cyclase-1 (GC1) knockout mouse. *PLoS One*. 2010;5:e11306.
105. Boye SE. Insights gained from gene therapy in animal models of retGC1 deficiency. *Front Mol Neurosci*. 2014;7:43.
106. Mihelec M, Pearson RA, Robbie SJ, et al. Long-term preservation of cones and improvement in visual function following gene therapy in a mouse model of leber congenital amaurosis caused by guanylate cyclase-1 deficiency. *Hum Gene Ther*. 2011;22:1179–1190.
107. Fine I, Wade AR, Brewer AA, et al. Long-term deprivation affects visual perception and cortex. *Nat Neurosci*. 2003;6:915–916.
108. Huber E, Webster JM, Brewer AA, et al. A lack of experience-dependent plasticity after more than a decade of recovered sight. *Psychol Sci*. 2015;26:393–401.
109. Jacobson SG, Cideciyan AV, Roman AJ, et al. Improvement and decline in vision with gene therapy in childhood blindness. *New Engl J Med*. 2015;372:1920–1926.

Investigative Ophthalmology & Visual Science

110. Cideciyan AV, Aleman TS, Boye SL, et al. Human gene therapy for RPE65 isomerase deficiency activates the retinoid cycle of vision but with slow rod kinetics. *Proc Natl Acad Sci U S A*. 2008;105:15112–15117.
111. Jacobson SG, Cideciyan AV, Ratnakaram R, et al. Gene therapy for leber congenital amaurosis caused by RPE65 mutations: safety and efficacy in 15 children and adults followed up to 3 years. *Arch Ophthalmol*. 2012;130:9–24.
112. Cideciyan AV, Hauswirth WW, Aleman TS, et al. Vision 1 year after gene therapy for Leber's congenital amaurosis. *New Engl J Med*. 2009;361:725–727.
113. Bennett J, Wellman J, Marshall KA, et al. Safety and durability of effect of contralateral-eye administration of AAV2 gene therapy in patients with childhood-onset blindness caused by RPE65 mutations: a follow-on phase 1 trial. *Lancet*. 2016; 388:661–672.

Investigative Ophthalmology & Visual Science